Electronic Supplementary Information (ESI)

Hydrazone-Linked DNP-Functionalized PLA Photocatalyst for Sustainable HAT-Mediated Hydroalkylation and NADH-Assisted Enzymatic CO_2-to- C_1 Fuel Conversion

Kanchan Sharma [a], Rajesh Kumar Yadav [a*], Rajesh Kumar Verma [b],Chandani Singh [c], Shaifali Mishra [a], Rehana Shahin [a], Jin-Ook Baeg [c*]

[a]*Department of Chemistry and Environmental Science, Madan Mohan Malaviya University of Technology, Gorakhpur, 273010, (U.P.), India. *Email: rkyches@mmmut.ac.in /rajeshkr_yadav2003@yahoo.co.in.

[b]Department of Mechanical Engineering, School of Engineering, Harcourt Butler Technical University, Kanpur, India- 208002

[c]*Korea Research Institute of Chemical Technology, N3, 141 Gajeong-ro, Yuseong-gu, Daejeon 34114, Korea South Korea. *Email: jobaeg@krict.re.kr;

Content

1. General remarks

Poly(lactic acid), 2,4-dinitrophenylhydrazine (DNP), chloroform, methanol, glacial acetic acid, ammonium chloride, nicotinamide adenine dinucleotide (NAD+), buffer solution, nitrogen gas, sodium tetraphenylborate, 4-bromobenzaldehyde, acrylamide, 2,4,6-tribromoaniline, acrylic acid, dimethylformamide (DMF), distilled water, diethyl ether, anhydrous sodium sulfate, ammonium tetraphenylborate (NH_4BPh_4),1,4-dioxane, acetonitrile, Rh compound ($[Rh(C_5Me_5)\ Cl_2]_2$), 2,2'-bipyridyl, ascorbic acid, all purchased from Sigma Aldrich and used in the reaction without further purification. The Rh complex and buffer solution was synthesized in the laboratory.

2. Instruments and measurements

The characterization of the synthesized material was carried out using various advanced analytical techniques. UV-DRS (UV-diffuse reflectance spectroscopy) and UV-Visible spectroscopy were recorded using a Shimadzu UV-1800 spectrometer. Fourier transform infrared (FTIR) spectroscopy was conducted with a Thermo Scientific Nicolet 6700 spectrometer, utilizing KBr pellets for sample support. The crystallographic structure was analyzed through powder X-ray diffraction (XRD) using a Bruker AXS D8 Advance diffractometer equipped with Cu Kα radiation.Morphological analysis was performed via scanning electron microscopy (SEM) using a Phillips FET instrument (Model No. 200kV LAB6, FEL TECNAI G2-20S-Twin) operating at 200 kV. Electrochemical measurements, including cyclic voltammetry (CV), electrochemical impedance spectroscopy (EIS), and Tafel plot analysis, were carried out on a CHI608E instrument. Proton nuclear magnetic resonance (1H NMR) spectra were obtained using a Bruker AVANCE II+ 300 MHz spectrometer, with tetramethylsilane (TMS; $\delta = 0$) as the internal reference. Additionally, X-ray photoelectron spectroscopy (XPS) analysis was conducted using a Thermo Fisher Escalab 250Xi instrument. XPS measurements were calibrated with reference to the C 1s peak at 284.8 eV. An atomic force microscope (AFM) (Bruker) was used to measure the surface morphology and height of the roughness of the synthesized materials and the HAADF-TEM were performed using Cs-TEM Spectra300. HPLC Analyses were performed on an Agilent HPLC system equipped with a C18 reverse-phase column.

Theoretical yields were calculated based on the limiting reagent, and isolated yields were determined accordingly. Formic acid yields were quantified using standard analytical calibration methods.

Theoretical yield:

Theoretical yield=(moles of limiting reagent)×(molar mass of product)

Percentage yield:

% Yield=[Actual (isolated) yield /Theoretical yield] ×100

3. X-ray Photoelectron Spectroscopy (XPS) analysis of DNP and DNPHz–PLA.

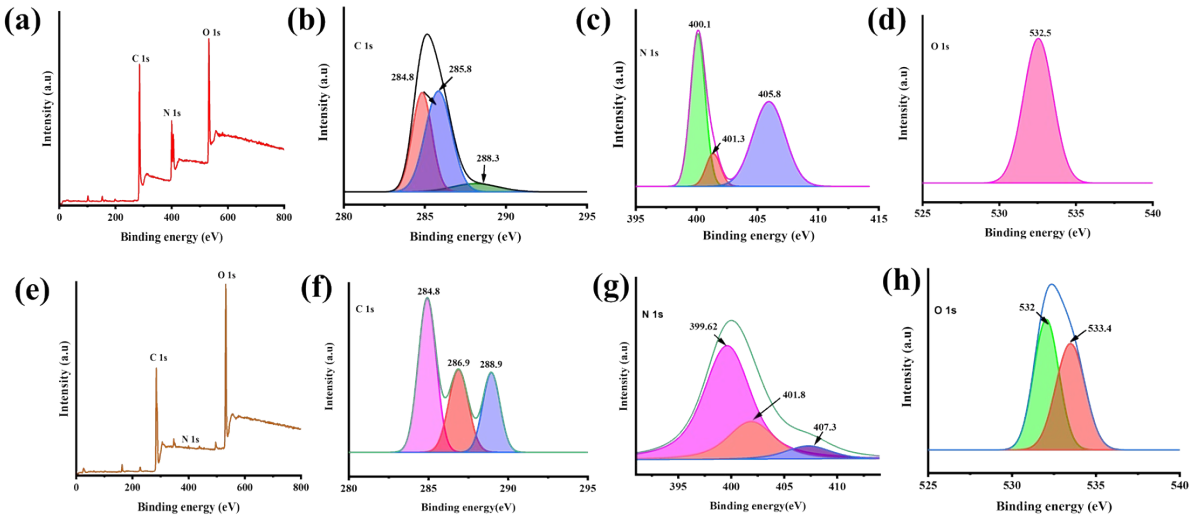

Figure S1. X-ray Photoelectron Spectroscopy (XPS) analysis of DNP and DNPHz–PLA. (a) Survey spectrum of DNP showing the presence of C, N, and O. (b) High-resolution C 1s spectrum of DNP displaying peaks at 284.8, 285.8, and 288.3 eV, (c) N 1s spectrum of DNP with peaks at 400.1, 401.3, and 405.8 eV, (d) O 1s spectrum of DNP showing a single prominent peak at 532.5 eV. (e) Survey spectrum of DNPHz–PLA, showing a relative decrease in N content and increase in C and O intensities due to incorporation of the PLA backbone. (f) High-resolution C 1s spectrum of DNPHz–PLA with peaks at 284.8, 286.9, and 288.9 eV, (g) N 1s spectrum of DNPHz–PLA showing peaks at 399.62, 401.8, and 407.3 eV, (h) O 1s spectrum of DNPHz–PLA displaying peaks at 532 and 533.4 eV.

4. Field Emission Scanning Electron Microscopy

The FESEM images of DNP Figure S2(a–d) clearly display a sheet-like, wrinkled, and lamellar morphology, which is typical of stacked aromatic domains. In contrast, PLA (e–h) exhibits a comparatively dense and compact surface with smooth block-like features, highlighting its polymeric aggregation. Upon formation of the DNPHZ–PLA composite (i–l), a distinct morphological transformation is observed, where the smooth PLA domains are replaced by a roughened and heterogeneous texture consisting of interconnected lamellae and fibrous structures. This clear difference in surface architecture confirms the successful incorporation of DNP into the PLA matrix, thereby validating the formation of DNPHZ–PLA.

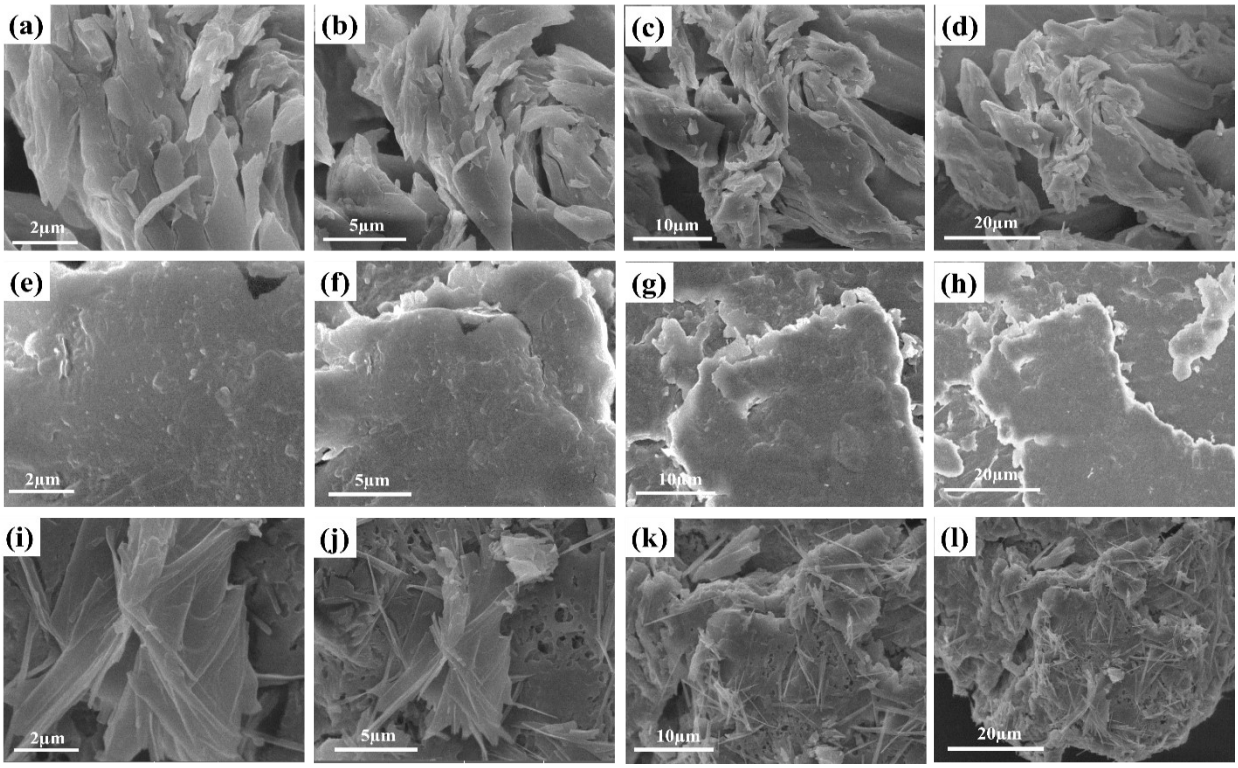

Figure S2: Field Emission Scanning Electron Microscopy (FESEM) images of (a–d) pristine DNP at different magnifications, (e–h) PLA, and (i–l) DNPHZ–PLA composite.

5. Tafel plots and linear fitting results along with Electrochemical impedance spectroscopy (EIS) results for DNP and DNPHz-PLA photocatalyst

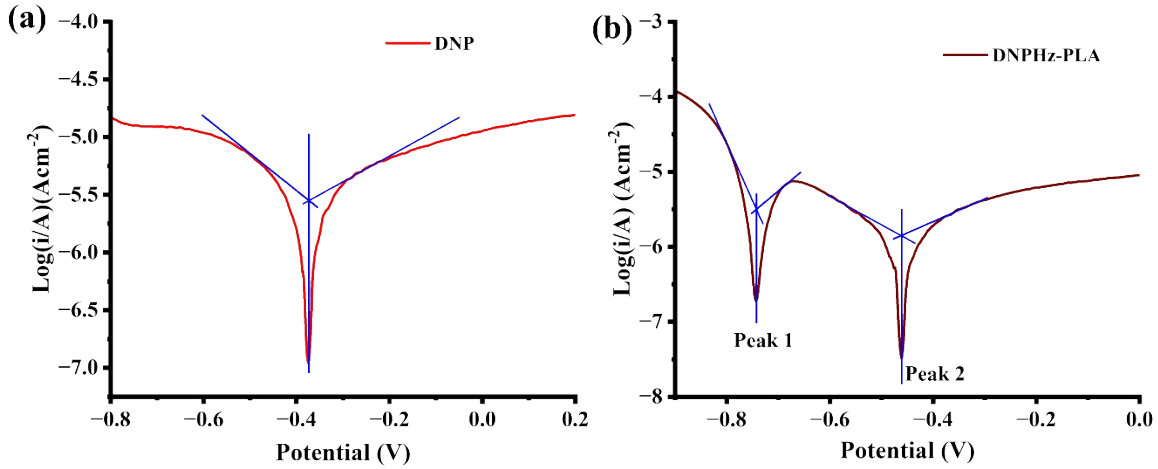

Material	E_{corr} (V)	βc(mV/dec)	βa(mV/dec)	I_{corr} (μA/cm²)
DNP	0.37	364	218	54.5
DNPHZ-PLA Peak 1	0.74	1627	584	54.9
DNPHZ-PLA Peak 2	0.46	335	209	58.5

Figure S3: Tafel plots and linear fitting results for (a) DNP, (b) DNPHZ-PLA (showing two peaks). Experimental data are presented as plots with the fitted linear regions overlaid. Extracted Tafel slopes (anodic β_a and cathodic βc) and corrosion parameters (E_corr, I_corr) for each material are summarized in the table. The data show that DNPHz-PLA exhibits lower Tafel slopes and improved corrosion parameters compared to DNP, indicating enhanced charge transfer kinetics due to the dual active sites in the DNPHz-PLA photocatalyst.

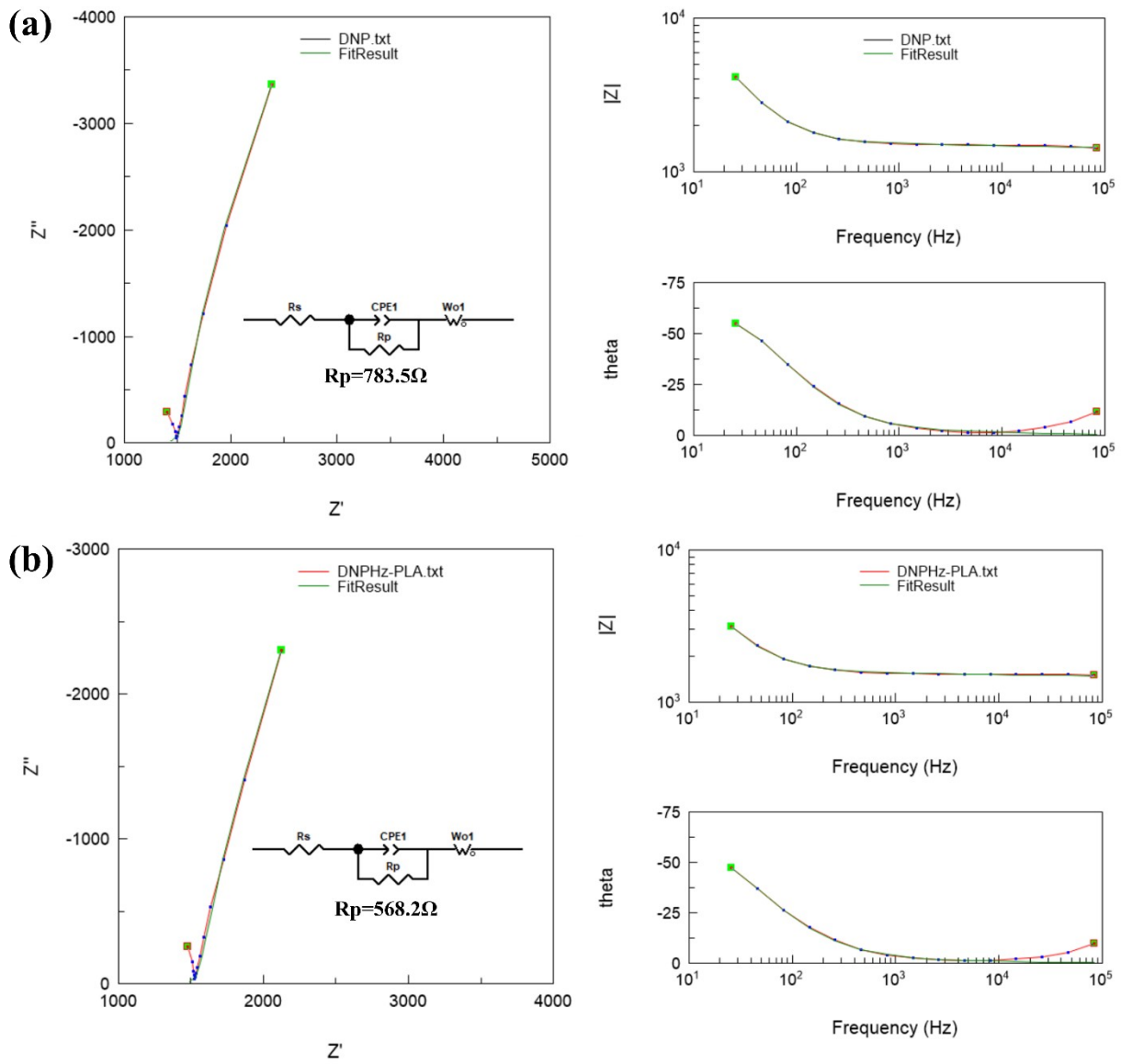

Figure S4. Nyquist plots (left), and Bode magnitude and phase plots (right) of EIS spectra for (a) DNP and (b) DNPHz-PLA photocatalyst. Experimental data are shown as scatter points with fitted curves obtained using ZView software. The equivalent circuit models used for fitting are shown as insets, incorporating solution resistance (Rs), charge-transfer resistance (Rp), constant phase element (CPE), and Warburg diffusion element (Wo), capturing both interfacial and diffusion-related processes. The excellent fitting confirms the suitability of the circuit model in describing the electrochemical behaviour of the DNP and DNPHz-PLA systems.

6. Rh-complex catalytic cycle for NADH regeneration using the DNPHz-PLA photocatalyst.

The proposed mechanism for photocatalytic NADH regeneration, illustrated in Figure S5, begins with photon absorption by the DNPHz-PLA photocatalyst. When the photon energy equals or exceeds the band gap of the photocatalyst, electron–hole pairs are generated within its valence band (VB), corresponding to the HOMO energy level (e.g., –6.0 eV in DNPHz–PLA). Ascorbic acid functions as a sacrificial electron donor by neutralizing the photogenerated holes in the VB/HOMO of the photocatalyst. This electron donation allows the photoexcited electrons to migrate into the conduction band (CB) or LUMO (–3.57 eV). From there, the electrons are transferred to a rhodium complex (Rh complex) with an energy level of 3.96 eV, supporting the progress of the photocatalytic cycle. Simultaneously, the cationic Rh species (a) in solution coordinates with water to form a hydrated intermediate (b), $[CpRh(bpy)(H_2O)]^{2+}$. Intermediate b undergoes β-hydrogen elimination with formate ($HCOO^-$), generated from ascorbic acid oxidation), yielding a rhodium hydride species (c), $[CpRh(bpy)(H)]^+$, along with CO_2 release. The photocatalyst (DNPHz–PLA) then donates its conduction band electron to this rhodium hydride intermediate, affording a reduced complex (d). Complex d subsequently transfers a hydride to NAD^+ at its amide group, thereby producing NADH.[1–5]

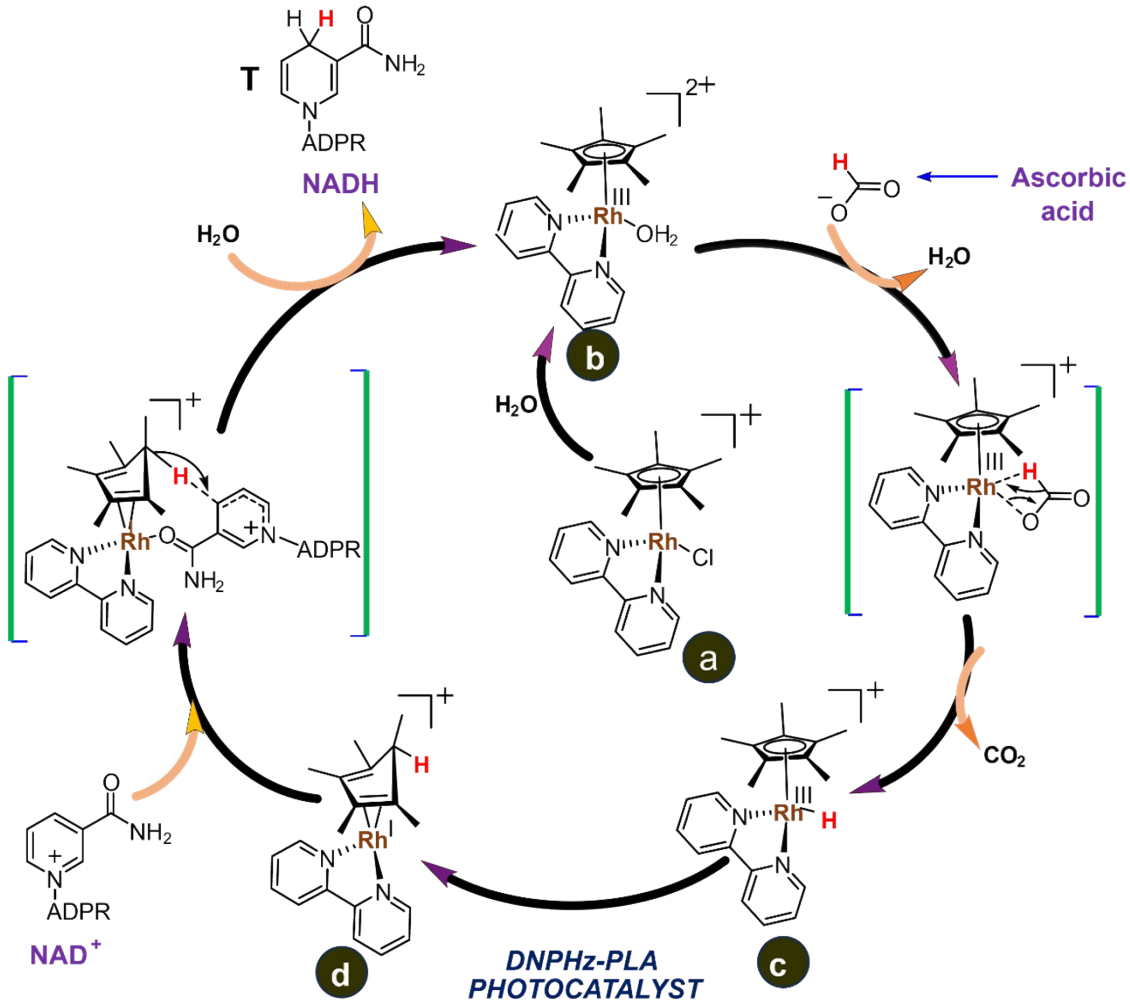

Figure S5. Schematic representation of the Rh-complex catalytic cycle for NADH regeneration mediated by the DNPHz-PLA photocatalyst.

7. Reusability and Physicochemical Stability of DNPHz-PLA Photocatalyst

The reusability of the DNPHz–PLA photocatalyst for NADH regeneration was evaluated by recovering the catalyst after each reaction cycle through filtration, followed by thorough washing with an excess of water. After drying, the photocatalyst was reused for multiple cycles. The reaction was repeated five times consecutively to assess the catalytic performance of the recovered DNPHz–PLA. As summarized in Figure S6(a), the photocatalytic efficiency of DNPHz–PLA remained high, with the yield decreasing only slightly from 73.8% in the first cycle to 64.47% after five runs, demonstrating good reusability. The physicochemical stability of the DNPHz–PLA photocatalyst for hydroalkylation of acrylamide was further analyzed using FTIR spectroscopy. After the first catalytic cycle, the recovered catalyst was washed, dried, and characterized. The FTIR spectra (Figure S6(b)) revealed that the characteristic absorption bands remained intact, though some peaks showed minor suppression, indicating preservation of the chemical structure. This confirms that DNPHz–PLA maintains its structural integrity after repeated use. Altogether, these results highlight the excellent reusability and stability of the DNPHz–PLA photocatalyst, ensuring consistent performance in hydroalkylation reactions over multiple cycles. [6–8]

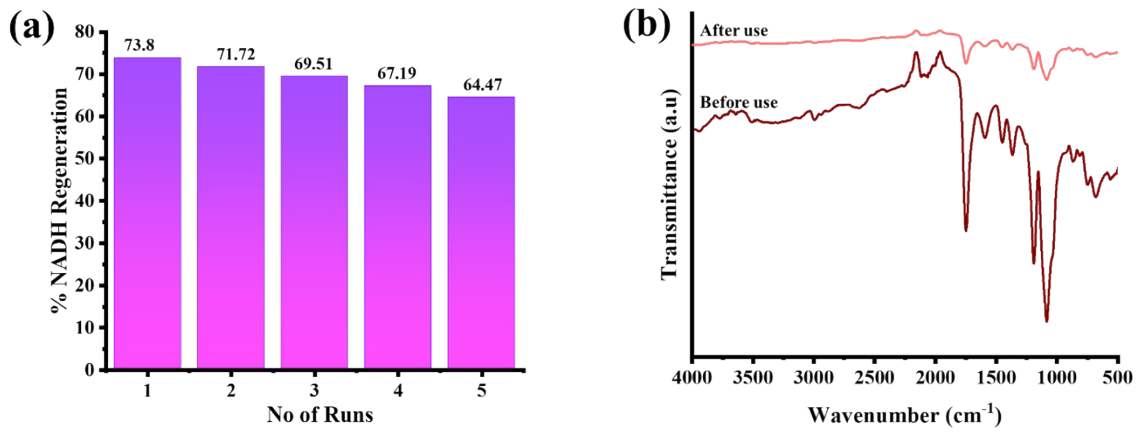

Figure S6 (a). Photocatalytic reusability and stability of the DNPHz–PLA photocatalyst in the NADH regeneration over five consecutive cycles. (b) FTIR spectra of the photocatalyst for hydroalkylation of acrylamide after the first catalytic cycle, indicating that the characteristic absorption bands remain intact, with minor suppression of some peaks, confirming structural integrity after use.

8. Hydrazone Bond Formation Mechanism of the DNPHz–PLA Photocatalyst and its 2D and 3D Schematic Representation.

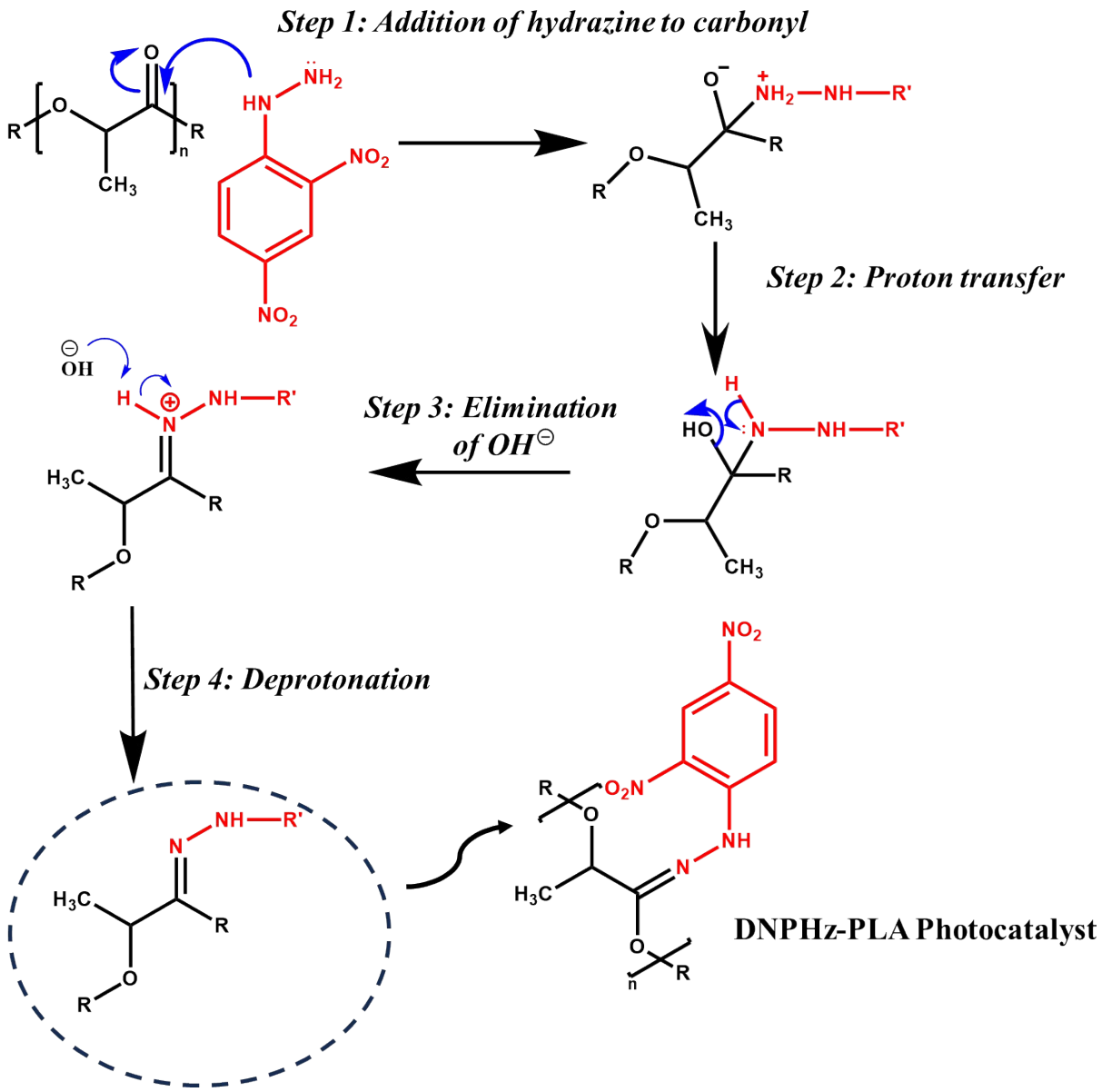

Figure S7. Proposed acid-catalyzed hydrazone bond formation mechanism between 2,4-dinitrophenylhydrazine (DNP) and carbonyl groups of PLA. The process involves protonation-assisted activation, nucleophilic interaction, proton transfer, and subsequent formation of a stable C=N–NH hydrazone linkage, resulting in covalent incorporation of DNP units into the PLA framework.

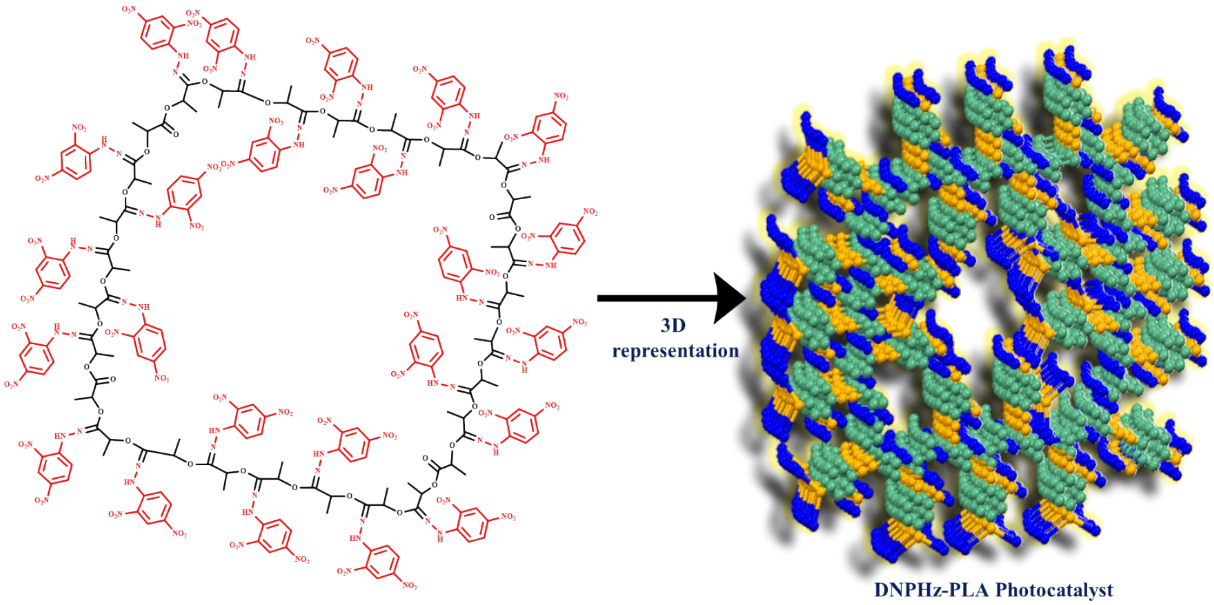

Figure S8. Schematic illustration of the 2D and 3D structure of the DNPHz–PLA photocatalyst. It is important to note that this representation is a simplified model for visualization purposes: not all C=O groups have been converted to hydrazone linkages, as confirmed by XPS, which shows the presence of residual C=O bonds, and EDS analysis, which indicates relatively low nitrogen content. This structural depiction is intended to provide a clearer conceptual understanding of the material rather than an exact depiction of all molecular features.

9. NMR Data Analysis of the Coupled Products

1H NMR spectra of 3-(4-formylphenyl)propanamide - 1H NMR (200MHz, CDCl3) δ 9.97 (s, 1H), 7.81 (d, 2H), 7.12 (d, 2H), 7.08 (d, 2H), 6.64 (s, 2H), 2.58 (d, 2H), 2.16 (d, 2H).

1H NMR spectra of 3-(4-formylphenyl)propanoic acid- 1H NMR (200MHz, CDCl3) δ 11.79 (s, 1H), 9.68 (s, 1H), 7.66 (d, 2H), 7.16 (d, 2H), 2.69 (t, 2H), 2.54 (t, 2H).

1H NMR spectra of 3,3',3''-(2-aminobenzene-1,3,5-triyl)tripropanamide-1H NMR (200MHz, CDCl3) δ 7.47 (s, 6H), 6.62 (s, 2H), 5.14 (s, 2H), 2.94–2.87 (m, 6H), 2.58 (t, 6H).

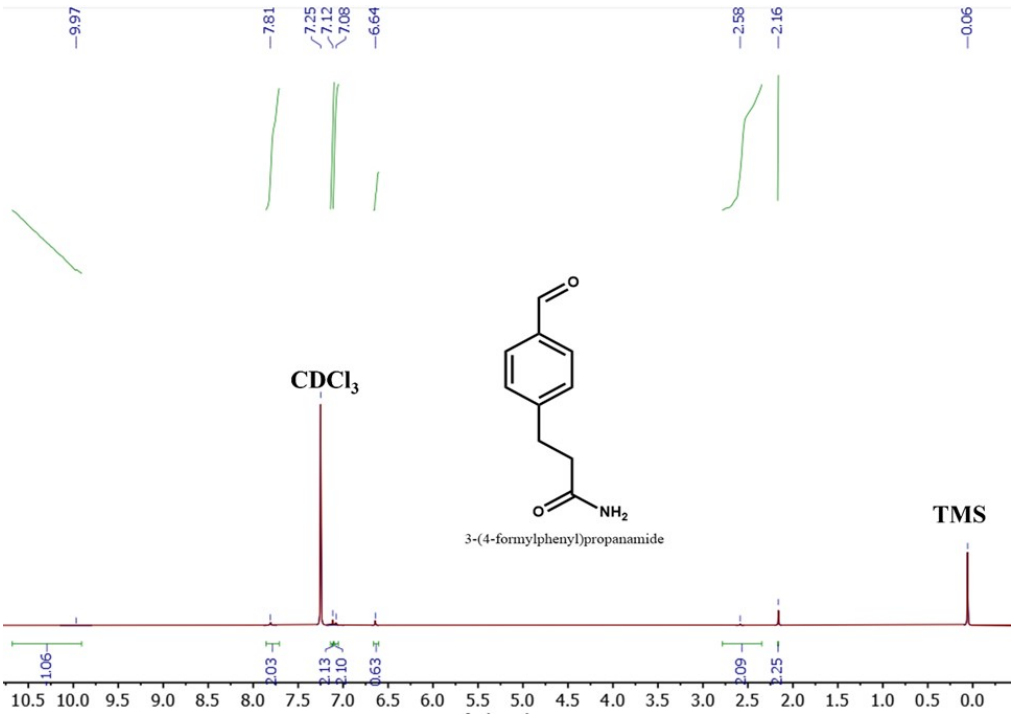

Figure S9. 1H NMR spectra of 3-(4-formylphenyl)propanamide.

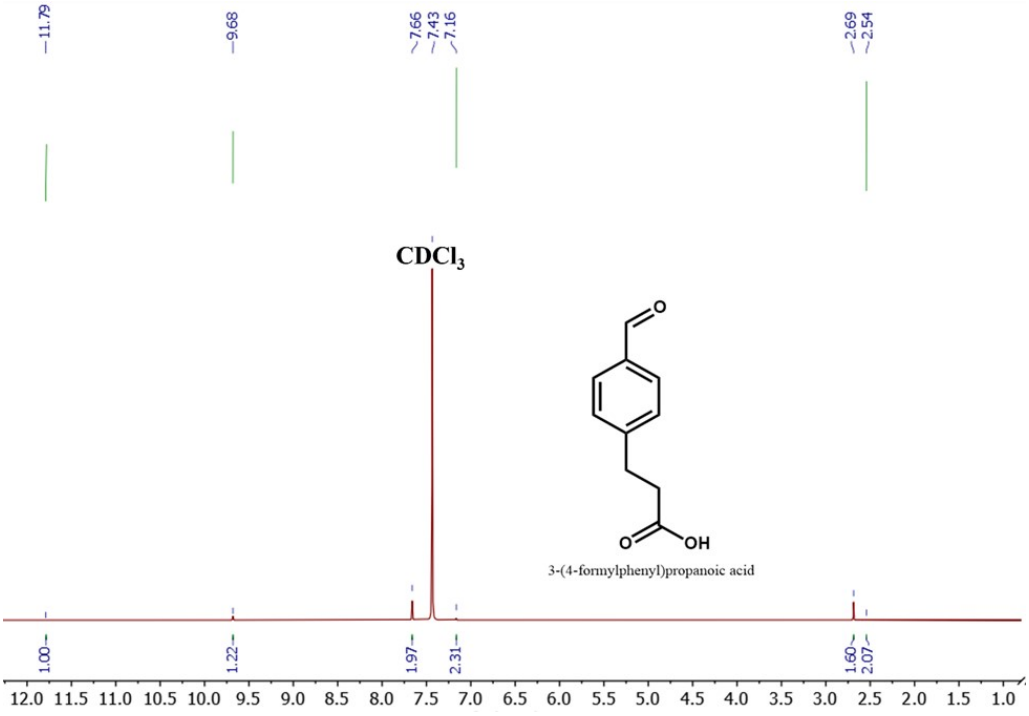

Figure S10. 1H NMR spectra of 3-(4-formylphenyl)propanoic acid.

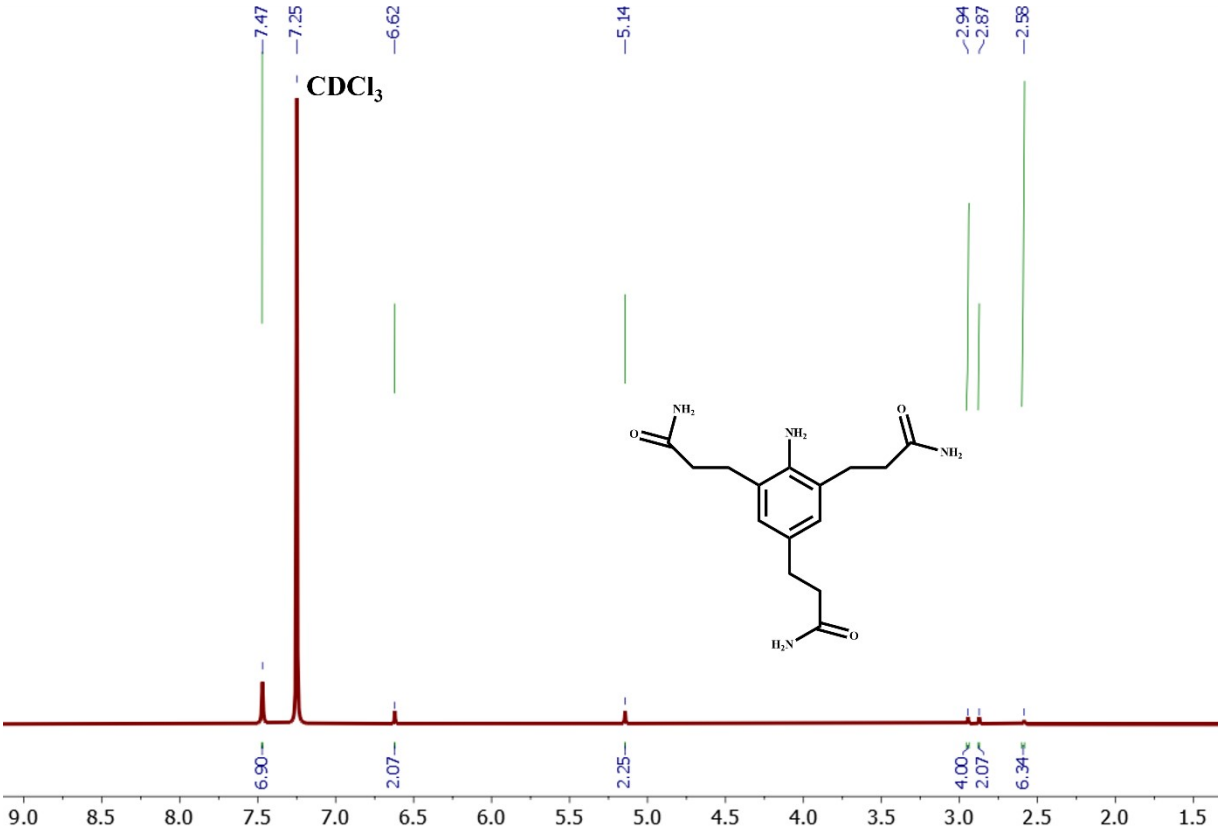

Figure S11. 1H NMR spectra of 3,3',3''-(2-aminobenzene-1,3,5-triyl)tripropanamide.

10. HPLC Analysis Confirming Photocatalytic CO_2-to-Formic Acid Conversion

HPLC analysis of formic acid was performed on a reverse-phase C18 column using a mobile phase of 80% water : 20% acetonitrile (v/v) at a flow rate of 1.0 mL min^{-1}. The injection volume was 5 µL, and detection was carried out at 550 nm. Figure S10 compares HPLC chromatograms of (a) a pure HCOOH acid and (b) the reaction sample. The standard produced a peak at 12.568 min, while the reaction mixture showed a major peak at 11.823 min, consistent with the presence of formic acid in the sample. Quantification by the calibration curve gave a formic acid production of 180.61 µmol.The slight retention time shift (~0.745 min) and the minor shoulder observed on peak (b) are attributed to matrix effects and co-eluting species from the reaction mixture (buffer components, or other small organics). These matrix influences can alter analyte partitioning and apparent retention times, and may produce small unresolved peaks or peak asymmetry.[9–11] For quantitative analysis, an external calibration curve was constructed over the concentration range of 10–140 mM (Figure S10 c). The linear regression equation obtained was:

$$y = 18.34744 + 0.72349x$$

where *y* represents the peak area (mAU) and *x* is the concentration (mM). The calibration displayed excellent linearity with an R^2 value of 0.99775. The reaction sample showed a peak area of 61.91 mAU, corresponding to a concentration of 60.20 mM based on the calibration curve, yielding a total formic acid production of 180.61 µmol in 3 mL.[12]

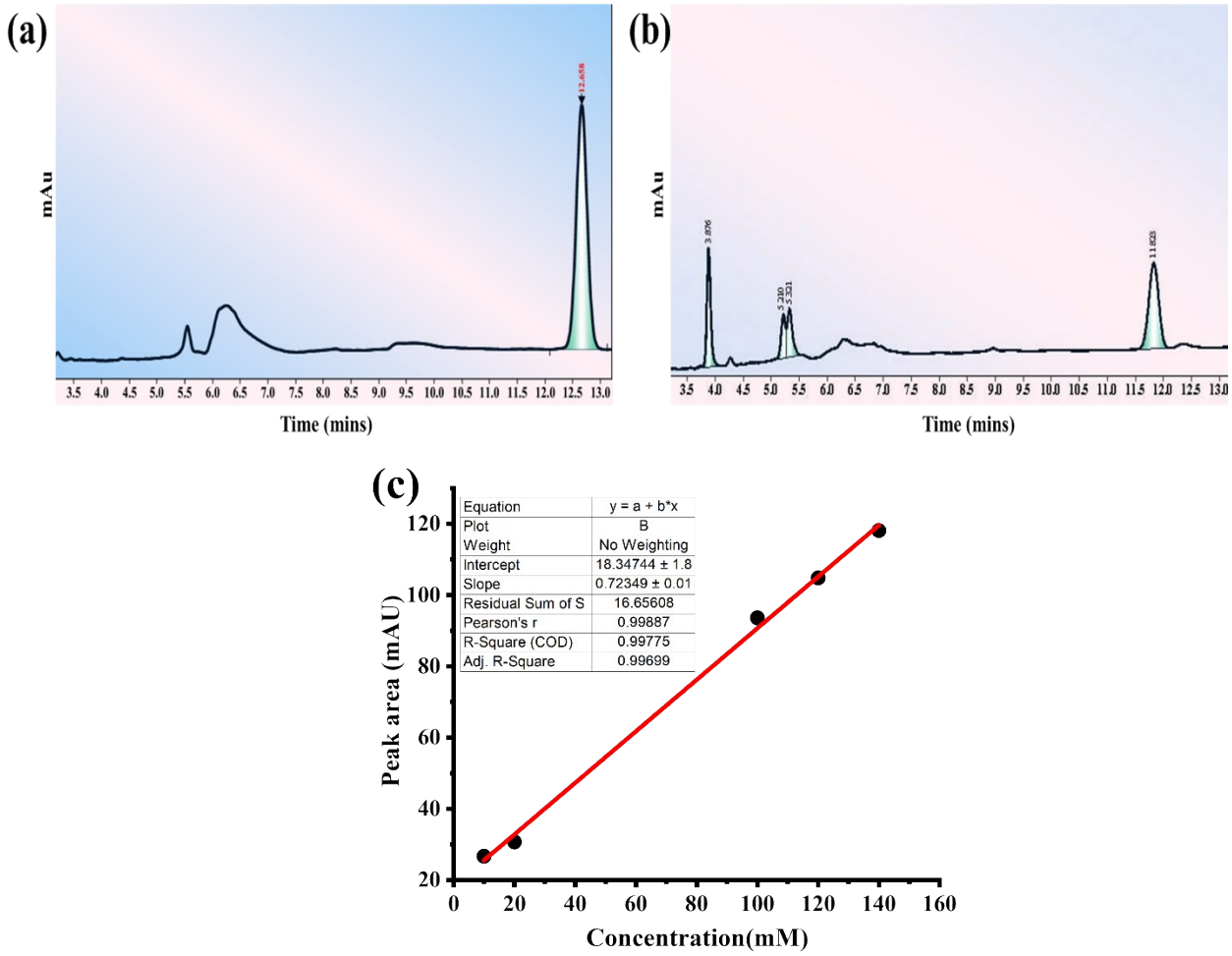

Figure S12. (a) Chromatogram of pure formic acid standard showing the characteristic peak at 12.568 min, used as a retention-time reference. (b) Chromatogram of the reaction mixture after photocatalytic CO_2 reduction using DNPHz–PLA–FDH system, displaying a major peak at 11.823 min corresponding to formic acid formed in the reaction. (c) standard curve of formic acid measured by HPLC.

References

1 B. Tan, D. P. Hickey, R. D. Milton, F. Giroud and S. D. Minteer, *J. Electrochem. Soc.*, 2015, **162**, H102–H107.

2 Z. Jiang, C. Lü and H. Wu, *Ind. \& Eng. Chem. Res.*, 2005, **44**, 4165–4170.

3 P. Singh, R. K. Yadav, K. Kumar, Y. Lee, A. K. Gupta, K. Kumar, B. C. Yadav, S. N. Singh, D. K. Dwivedi, S. H. Nam, A. P. Singh and T. W. Kim, *Catal. Sci. Technol.*, 2021, **11**, 6401–6410.

4 Y. Zhang, Y. Zhao, R. Li and J. Liu, 2020, **2000339**, 1–18.

5 V. Gupta, R. K. Yadav, A. Umar, A. A. Ibrahim, S. Singh, R. Shahin, R. K. Shukla, D. Tiwary, D. K. Dwivedi, A. K. Singh, A. K. Singh and S. Baskoutas, *Catalysts*, , DOI:10.3390/catal13040666.

6 S. K. B. Rajesh K. Yadav, Jin-Ook Baeg, Gyu Hwan Oh, No-Joong Park, Ki-jeong Kong, Jinheung Kim, Dong Won Hwang, R. K. Yadav, J. O. Baeg, G. H. Oh, N. J. Park, K. J. Kong, J. Kim, D. W. Hwang and S. K. Biswas, *J. Am. Chem. Soc.*, 2012, **134**, 11455–11461.

7 S. Srivastava, R. K. Yadav, S. Singh, R. Shahin, A. P. Singh, N. K. Gupta, T. W. Kim and J. O. Baeg, *J. Chem. Sci.*, , DOI:10.1007/s12039-023-02223-9.

8 M. Singh, R. K. Yadav, S. Mishra, R. Shahin, S. Singh, R. Singhal, N. K. Gupta, J. O. K. Baeg, G. A. El-Hiti and K. Kumar Yadav, *ChemistrySelect*, 2024, **9**, 1–10.

9 K. Sharma, R. K. Yadav, S. Singh, C. Singh, R. Shahin, K. Kumar, R. K. Verma, D. K. Dwivedi, J.-O. Baeg and N. K. Gupta, *Mol. Catal.*, 2023, **548**, 113379.

10 Y. Nishiwaki-Akine and T. Watanabe, *Green Chem.*, 2014, **16**, 3569–3579.

11 S. Lee, H. Ju, H. Jeon, R. L. Machunda, D. Kim, J. K. Lee and J. Lee, *ECS Trans.*, 2013, **53**, 41–47.

12 P. Fan, L. Zhang, Z. Liu, W. Zhang, Q. Cui and H. Wang, 2020, 843–850.